Granular flow in a wedge-shaped hopper with smooth walls and radial gravity: Theory and simulations

Afroz F. Momin and Devang V. Khakhar*
Department of Chemical Engineering, Indian Institute of Technology Bombay, Powai, Mumbai 400076, India

(Received 12 June 2024; accepted 5 March 2025; published 31 March 2025)

Hoppers with inclined walls are commonly used in industrial applications to facilitate the gravity-driven discharge of materials through a bottom outlet. The simplest form of this flow configuration, a wedge-shaped, quasi-two-dimensional hopper with frictionless walls and a gravitational force radially directed toward the apex of the wedge, is considered. A closed form solution of the flow was given in the classical work of Savage [Br. J. Appl. Phys. **16**, 1885 (1965)]. Discrete element method (DEM) simulations are performed to analyze the stress and velocity fields for granular flow in a close replica of the system considered in the theory. Results are presented for varying hopper parameters (orifice size and wedge angle) and particle properties (particle diameter, friction coefficient, and stiffness). A detailed comparison of the computational results with the predictions of the Savage model indicates that the model predicts the stress accurately, except near the exit, but predicts velocities significantly higher than the computational values. The deviation is due to the assumption that the stress at the exit is zero, which is contrary to the significant exit stress obtained from computations. The flow is purely extensional and is found to follow the μ-I rheology, which includes frictional and collisional stresses. A flow model based on the μ-I rheology is presented, and model predictions of the stress and solid fraction profiles closely match the computational results. Correlations for the velocity and the mass flow rate, in terms of the system parameters, are obtained from the simulation data.

DOI: 10.1103/PhysRevFluids.10.034303

I. INTRODUCTION

Hoppers are important components in most granular processes in industry, being used for storage as well as a means of feeding granular material [1]. The stress distribution and flow patterns in hoppers are of considerable importance for the design and operation of hoppers and have been widely studied, starting with the pioneering works of Brown and Richards [2], Beverloo *et al.* [3] and Jenike [4]. A detailed review of the mass flow rate from hoppers is given by Nedderman *et al.* [5], and a key result is the Beverloo correlation [3] given for a two-dimensional system by

$$\dot{m} = C\rho^{1/2} g b (d_0 - a_1 d_p)^{3/2}, \tag{1}$$

where ρ is the bulk density, g is the acceleration due to gravity, b is the thickness of the hopper, d_0 is the orifice width, d_p is the particle diameter, and C and a_1 are constants. The correlation is found to be valid for many different systems and indicates that the flow rate is dependent primarily on the width of the orifice, occluded by a couple of layers of static particles near the edge of the orifice. Thus, the mass flow rate is determined entirely by the flow in a small region near the exit, which has been the subject of several studies [6,7]. Comprehensive accounts of the flow fields,

*Contact author: khakhar@iitb.ac.in

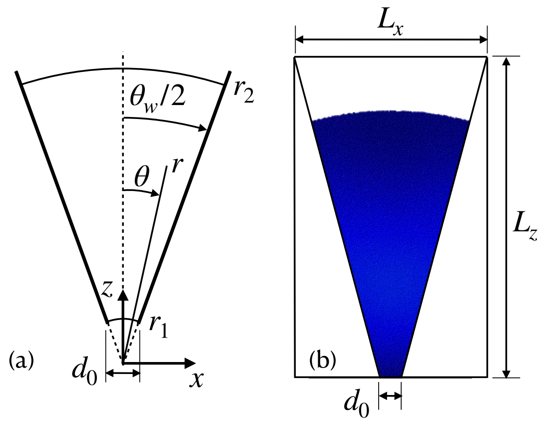

FIG. 1. (a) Schematic view of a wedge-shaped hopper showing the coordinate system and geometrical dimensions. The shaded area shows the bin used for averaging with volume $V = (r\theta_w) \times d_p \times L_y$. (b) Snapshot of system used in the simulation studies.

stress distributions, and practical design aspects related to bins and hoppers are given in the books by Nedderman [8] and Schulze [1]. Authors of several recent studies have examined the role of geometry and particle properties on the flow rate and flow patterns from hoppers [9–13]. The orifice for outflow in feed hoppers is typically much smaller than the hopper diameter, resulting in a strongly converging flow. The flows have thus been used as a test bed for granular rheology models [14,15].

Hoppers used for feeding granular material have a conical or wedge-shaped lower portion to facilitate the flow and prevent the formation of stagnant regions. The focus of this paper is on wedge shaped hoppers. The stress distribution and flow in such hoppers was studied by Jenike [4], neglecting intertia effects. Savage [16] considered a simplified version of the problem, assuming the hopper walls to be frictionless and the gravitational force to be radially directed but included inertial stresses, and obtained a closed-form solution for the problem. However, the predicted flow rates were 37–82% higher than experimental values for the range of wedge angles considered [16]. To our knowledge, the Savage [16] theory is the only exact solution to a nontrivial granular flow. Savage [17], Brennen and Pearce [18], Kaza and Jackson [19], and Savage and Sayed [20] considered wedge wall friction and showed that including wall friction gave flow rates close to those obtained experimentally. In all these studies, the constitutive relation for the granular flow was used was the Mohr-Coulomb yield condition, taking the flow to be of constant density. Using the Mohr-Coulomb yield condition implies that the stresses are purely frictional and hence are independent of the velocity. Consequently, the flow rate is determined by the inertial resistance in the flow, as elaborated in the next section. In some cases, the condition of colinearity between stress and strain rate was also imposed [4,18,19]. Prakash and Rao [21] used the critical state theory [22] to account for compressibility effects in the smooth wall radial gravity problem. The flow rates are again determined by the inertial resistance of the material since stresses in the critical state theory are velocity independent. Jyotsna and Rao [23] analyzed the problem using a frictional-kinetic theory and found that granular temperatures are high near the exit of the hopper, implying significant viscous effects, which arise from interparticle collisions. The flow rate in this case is determined by both inertial and viscous resistances. None of the theories discussed above predict the dependence of mass flow rate on particle diameter, as in the Beverloo [3] correlation [Eq. (1)].

In this paper, we use the discrete element method (DEM) to carry out extensive simulations of the canonical system studied by Savage [16]: a wedge-shaped hopper with frictionless side walls and gravity acting radially [Fig. 1(a)]. One objective of this paper is to analyze the validity of the assumptions and predictions of the Savage [16] model using the simulation results. The simulation procedure is designed to precisely replicate the assumptions in the theory, which is difficult in an experimental system. Another objective is to understand the rheological behavior of the converging flow in the wedge, which is shown below to be a pure extensional flow. Such flows are qualitatively different from granular shear flows, that have been studied previously in depth. A parametric study is carried out varying the hopper geometry (orifice width d_0, wedge angle θ_w, and fill height r_2) and particle properties (diameter d_p, friction coefficient μ_p, and stiffness k_n). The simulation results are compared with the Savage [16] theory and to a theory based on the μ-I rheology [24], which is shown to be valid for the flow. The paper is organized as follows. In Sec. II, the theory is discussed; Sec. III outlines the simulation methodology; Sec. IV presents the results; and Sec. V gives conclusions of this paper.

II. THEORY

We first present a review of the Savage [16] theory and then, following a similar approach, analyze the problem assuming the material to follow the μ-I rheology [24].

A. Savage model

The Savage [16] model is based on the following assumptions: (i) The bulk density (ρ) is constant throughout the hopper; (ii) the Mohr-Coulomb condition is satisfied at all points; (iii) the walls of the hopper are frictionless; and (iv) gravity acts radially. As a consequence of assumptions (iii) and (iv), all variables are independent of θ [Fig. 1(a)], and the shear stress is zero ($\sigma_{r\theta} = 0$). The latter implies that σ_{rr} and $\sigma_{\theta\theta}$ are principal stresses, and the Mohr-Coulomb condition becomes

$$\frac{\sigma_{\theta\theta}}{\sigma_{rr}} = \frac{1 + \sin\beta_s}{1 - \sin\beta_s} = k, \tag{2}$$

where β_s is the angle of internal friction, and k is the stress ratio. Equation (2) should more correctly be referred to as the Shield-Jenike equation [25] since the Mohr-Coulomb condition is valid only at the yield point. Jenike and Shield [25] showed through extensive experimentation that Eq. (2) is valid beyond yield for slow shearing but with k significantly larger than the yield value [25].

Using the assumptions given above, the continuity equation for the flow becomes

$$\frac{d}{dr}(r v_r) = 0, \tag{3}$$

which yields the radial velocity as

$$v_r = -A/r, \tag{4}$$

where A is a constant to be determined. The r-momentum balance equation reduces to

$$\rho v_r \frac{dv_r}{dr} = -\frac{d\sigma_{rr}}{dr} - \frac{\sigma_{rr} - \sigma_{\theta\theta}}{r} - \rho g, \tag{5}$$

where g is the acceleration due to gravity acting radially. The θ-momentum balance is identically satisfied. Upon substitution of v_r and $\sigma_{\theta\theta}$ using Eqs. (2) and (4), we get

$$\frac{d\sigma_{rr}}{dr} - (k-1)\frac{\sigma_{rr}}{r} = -\rho g + \frac{\rho A^2}{r^3}, \tag{6}$$

which has the solution

$$\sigma_{rr} = -\frac{\rho g r}{2-k} - \frac{\rho A^2 r^{-2}}{k+1} + B r^{k-1}, \tag{7}$$

where B is a constant of integration. The velocity dependence of the stress is due to the inertial term [second term in Eq. (7)]. If inertia is negligible, the stress becomes independent of the velocity; the boundary condition at $r = r_1$ cannot be satisfied; and A and, consequently, the mass flow rate are indeterminate. Savage [16] utilized the boundary conditions $\sigma_{rr} = 0$ at $r = r_1$ and r_2 to determine the constants A and B, which are given by

$$A = \left\{ \frac{g(k+1){r_1}^3}{(k-2)} \left[\frac{1-(r_1/r_2)^{(k-2)}}{1-(r_1/r_2)^{(k+1)}} \right] \right\}^{1/2}, \tag{8}$$

$$B = \frac{1}{r_1^{k-1}} \left[\frac{\rho g r_1}{2-k} + \frac{\rho A^2 r_1^{-2}}{k+1} \right]. \tag{9}$$

The mass flow rate in the hopper is

$$\dot{m} = \rho A \theta_w b, \tag{10}$$

which can be obtained in terms of the system parameters using Eq. (8). Substituting for the constants A and B using Eqs. (8) and (9), the normal stress in the r direction is obtained as

$$\sigma_{rr} = \frac{\rho g r}{k-2} \left[1 - \left(\frac{r}{r_2} \right)^{(k-2)} \right] - \frac{\rho g r_1^3}{(k-2) r^2} \left[1 - \left(\frac{r}{r_2} \right)^{(k+1)} \right] \left[\frac{1-(r_1/r_2)^{(k-2)}}{1-(r_1/r_2)^{(k+1)}} \right], \tag{11}$$

and in the θ direction, it is $\sigma_{\theta\theta} = k\sigma_{rr}$.

B. μ-I model

Authors of previous studies [23,26] have shown that the rheology near the exit of the hopper is not purely frictional, as assumed in the Savage [16] model, but also has a viscous contribution resulting from interparticle collisions. We use the frictional-collisional μ-I model [24], according to which the stress components are

$$\boldsymbol{\sigma} = P\mathbf{I} - 2\eta\mathbf{D}, \tag{12}$$

where P is the pressure, η is the viscosity, and $\mathbf{D}$ is the rate of strain tensor. From Eq. (4), $D_{rr} = dv_r/dr = A/r^2$, $D_{\theta\theta} = v_r/r = -A/r^2$, and $D_{r\theta} = 0$; hence, the flow is purely extensional. Further, $\sigma_{r\theta} = 0$ since $D_{r\theta} = 0$, implying that σ_{rr} and $\sigma_{\theta\theta}$ are principal stresses. For the μ-I model [24], the viscosity is given by

$$\eta = \frac{\mu P}{\dot{\gamma}}, \tag{13}$$

where $\dot{\gamma} = (2\mathbf{D} : \mathbf{D})^{1/2}$ is the shear rate, $\mu = \mu(I)$ is the shear-rate-dependent friction coefficient, and I is the inertial number given by

$$I = \dot{\gamma} d_p \left(\frac{\rho_p}{P} \right)^{1/2}, \tag{14}$$

where ρ_p is the particle density, and d_p is the particle diameter. The empirical function $\mu(I)$ is obtained from the simulation data.

Using Eq. (4), we get $\dot{\gamma} = 2A/r^2$, and substituting for η, $\mathbf{D}$, and $\dot{\gamma}$ in Eq. (12), we get

$$\sigma_{rr} = P(1-\mu), \tag{15}$$

$$\sigma_{\theta\theta} = P(1+\mu). \tag{16}$$

From the above equations, we get

$$\frac{\sigma_{\theta\theta}}{\sigma_{rr}} = \frac{1+\mu}{1-\mu} = k_d, \tag{17}$$

and $P = (\sigma_{rr} + \sigma_{\theta\theta})/2$. Thus, in this flow, $\mu = \sin\beta$, where $\beta(I)$ is the shear-rate-dependent angle of internal friction. Equation (17) is equivalent to a modified Shield-Jenike equation (Mohr-Coulomb condition), and consequently, the governing equations for the μ-I model are identical to the Savage [16] model [Eqs. (4) and (6)] but with k replaced by $k_d(I)$ in the stress equation [Eq. (6)] as

$$\frac{d\sigma_{rr}}{dr} - (k_d - 1)\frac{\sigma_{rr}}{r} = -\rho g + \frac{\rho A^2}{r^3}. \tag{18}$$

The μ-I model reduces to the Savage [16] model in the limit $I \to 0$. Even when inertia is negligible [$\rho A^2/r^3 \approx 0$ in Eq. (18)], the stress depends on the shear rate through $k_d(I)$, in contrast with the Savage [16] model in which the stress is independent of shear rate in this limit.

Equation (18) is nonlinear and requires a numerical solution. However, if we assume that k_d varies slowly with r, we obtain the following approximate solution:

$$\sigma_{rr} = \frac{\rho g r}{k_d - 2}\left[1 - \left(\frac{r}{r_2}\right)^{k_d-2}\right] - \frac{\rho A^2}{r^2(k_d+1)}\left[1 - \left(\frac{r}{r_2}\right)^{k_d+1}\right] \tag{19}$$

using $\sigma_{rr} = 0$ at $r = r_2$. Equation (19) is identical to Eq. (11) but with k replaced by $k_d(I)$. The computational results given in Sec. IV D indicate that $\sigma_{rr}(r_1) > 0$. We, thus, use only the boundary condition at the free surface ($\sigma_{rr} = 0$ at $r = r_2$) and treat A as a fitting parameter, which is obtained by fitting Eq. (4) to the computed velocity profile. We present results for Eq. (19) and results from numerical integration of Eq. (18) using the boundary condition $\sigma_{rr} = 0$ at $r = r_2$ and the fitted value of A for both.

In the case of no flow ($A = 0$), both models yield the following expression for the stress:

$$\sigma_{rr} = \frac{\rho g r}{k - 2}\left[1 - \left(\frac{r}{r_2}\right)^{k-2}\right]. \tag{20}$$

The profile only satisfies the boundary condition $\sigma_{rr}(r_2) = 0$, and the stress increases monotonically with depth. This is also the profile for the Savage [16] model when inertia is neglected. For $k = 1$, we get a hydrostatic variation of the stress with depth given by $\sigma_{rr} = \rho g(r_2 - r) = \sigma_{\theta\theta}$.

III. SIMULATION METHODOLOGY

Simulations were carried out using the DEM with polydisperse soft particles ($\pm 10\%$ size polydispersity) having a mean diameter $d_p = 1$ mm and a mass density $\rho_p = 2.5\ \mathrm{g/cm^3}$, using LAMMPS [27]. A schematic representation of the system is shown in Fig. 1 along with the computational domain, where d_0 is the orifice width and the dimensions of the computational domain are $L_z = r_2' + 6$ cm, $L_x = 2L_z\tan(\theta_w/2) + d_0$, and $L_y = 1.0$ cm. To achieve the same boundary condition as in the Savage [16] theory, the top surface is shaped to be an arc of a circle with radius $r = r_2'$, and the values used are given below.

The Hookean linear spring-dashpot model with velocity-dependent damping was used. The contact force model incorporates elastic normal and tangential components and viscous damping only in the normal direction. The Coulomb friction criterion was used, which limits the tangential force to the product of the particle friction coefficient (μ_p) and the normal force. The model used along with the parameter values for the base case (S_2), presented in Table I, corresponds to the L3 model proposed by Silbert *et al.* [28]. The values of the dissipation constant γ_n used correspond to a coefficient of restitution $e = 0.88$. A body force $(-mg\sin\theta,\ 0, -mg\cos\theta)$ was imposed on each particle, where m is the mass of the particle, and θ is the angular position of the particle. This is equivalent to a radial gravity force. The walls of wedge are frictionless and inelastic ($e = 0.88$) with the same value of stiffness (k_n) as the particles. The Verlet integration algorithm was used with a time step of $dt = 10^{-6}$ s, which is equal to $t_{\mathrm{col}}/50$, where t_{col} is the binary collision time for a pair particles undergoing a head-on collision [28]. The simulations were stable in all cases, and further reduction in the time step did not alter the results.

The steps used in the simulations are shown in Fig. 2. Particles are poured for a time duration of 1 s (1 million time steps) on an existing bed of particles to achieve a height in the bin greater than

TABLE I. List of the systems used in the simulations for studying the effects of orifice width (d_0), wedge angle (θ_w), friction coefficient (μ_p), stiffness (k_n), damping coefficient (γ_n), radial distance (r_2), and particle diameter (d_p).

Systems	Orifice width d_0 (cm)	Wedge angle θ_w (deg.)	Friction coefficient μ_p (-)	Normal stiffness k_n (dyn/cm)	Damping coefficient γ_n (1/s)	Timestep dt (s)
S_2 (base case)	0.8	30°	0.5	2 568 000	4952	1×10^{-6}
S_1–S_5	0.6–1.4	30°	0.5	2 568 000	4952	1×10^{-6}
S_6–S_9	0.8	20°–60°	0.5	2 568 000	4952	1×10^{-6}
S_{10}–S_{17}	0.8	30°	0.0–1.0	2 568 000	4952	1×10^{-6}
S_{18}	0.8	30°	0.5	25 680 000	15 661	3.18×10^{-7}
S_{19}	0.8	30°	0.5	256 800 000	49 525	1×10^{-7}
S_{20}	1.0	37.8°	0.5	2 568 000	4952	1×10^{-6}
S_{21}	1.2	45.7°	0.5	2 568 000	4952	1×10^{-6}
S_{22}	0.8	23.9°	0.5	2 568 000	4952	1×10^{-6}
S_{23}	0.8	19.9°	0.5	2 568 000	4952	1×10^{-6}
S_{24}–S_{27} (r_2 : 9–21)	0.8	30°	0.5	2 568 000	4952	1×10^{-6}
S_{28} (d_p : 1.5)	0.8	30°	0.5	5 778 567	4044	1.23×10^{-6}
S_{29} (d_p : 2.0)	0.8	30°	0.5	10 273 008	3502	1.42×10^{-6}
S_{30} (d_p : 2.5)	0.8	30°	0.5	16 051 575	3132	1.59×10^{-6}
S_{31} (d_p : 3.0)	0.8	30°	0.5	23 114 268	2859	1.74×10^{-6}

r_2' and allowing sufficient time for all particles to settle [Figs. 2(a) and 2(b)]. Next the top surface is shaped into an arc by removing all particles with $r > r_2'$ [Fig. 2(c)]. The system is then allowed to run for 0.15 s (0.15 million time steps) to attain equilibrium. Subsequently, the orifice is opened, enabling particle discharge through the orifice [Fig. 2(d)]. After the flow achieves a steady state, data during flow are collected for a subsequent time interval during which ~3000 particles exit the hopper. The value of r_2' is taken so that free surface radius r_2 at the start of the data collection is $r_2 = r_1 + 10 \pm 0.1$ cm. This ensures that the height of material in the hopper ($r_2 - r_1$) is constant for the different cases, excluding those where the height is explicitly varied. The values of r_2' used are

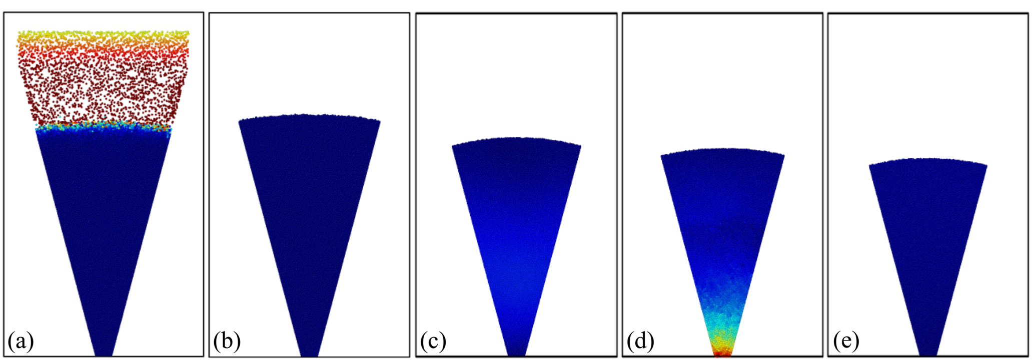

FIG. 2. Snapshots of the sequence of steps used in the simulations. (a) Refilling of particles by pouring. (b) Equilibration after pouring step. (c) Shaping the top surface to an arc of radius r_2 followed by equilibration. (d) Particle discharge on opening the exit and data collection after steady state is reached. (e) Equilibration after exit is closed and data collection in the static state.

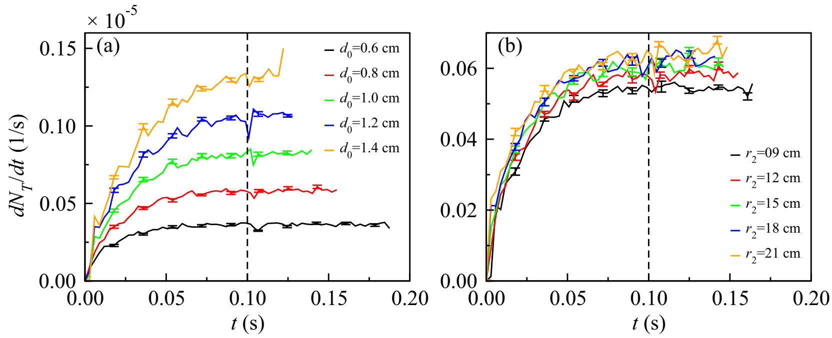

FIG. 3. Variation of the time rate of change of the number of particles in the hopper (dN_T/dt) with time (t) for varying system parameters. (a) Orifice width (d_0). (b) Height of material in the hopper (r_2). Parameters other than the one varied correspond to the base case: $d_0 = 0.8$ cm, $(r_2 - r_1) = 10$ cm, $\theta_w = 30^\circ$, $d_p = 0.1$ cm, $\mu_p = 0.5$, $k_n = 2.568\times10^6$ dyn/cm, and $\gamma_n = 4952$ 1/s.

in the range (10.3,11.1) cm. During the data collection, the change in height (r_2) is $\sim 5\%$ and may be assumed to be nearly constant. For the larger particles, the number of particles exiting during data collection is reduced to ensure that the height change is $\sim$5%. Finally, the orifice is closed, and the system is allowed to run for 0.1 s (0.1 million time steps) to establish a static steady state [Fig. 2(e)], followed by an additional duration of 0.05 s (0.05 million time steps) for data collection for the static bed. The data collected are averaged over 30 such simulation runs and up to 100 runs for cases involving larger size particles. We average over many samples ($\geqslant$30) to get very accurate results since we are comparing with an exact theory. The mean values are reported along with error bars, which indicate the standard error, calculated as the standard deviation divided by the square root of the number of samples.

Figure 3 shows the variation of the time rate of change of the number of particles in the hopper (dN_T/dt) with time (t), beginning at the start of the flow from rest, for different orifice widths (d_0) and filling heights (r_2). In all cases, the flow achieves a steady state (constant value of dN_T/dt) after $\sim$0.1 s. Slightly larger times were used in the simulations to ensure that the data were collected during steady flow from the hopper.

The parameters varied in the study are given in Table I and include the orifice width d_0 (0.6, 0.8, 1.0, 1.2, 1.4 cm), wedge angle θ_w (20°, 30°, 40°, 50°, 60°), particle diameter d_p (1.0, 1.5, 2.0, 2.5, 3.0 mm), friction coefficient μ_p (0.0, 0.1, 0.2, 0.3, 0.4, 0.5, 0.6, 0.7, 1.0), and stiffness values k_n corresponding to 1, 10, and 100 times the base case value. In the simulations with different particle diameters (d_p), the thickness of the hopper was varied with $L_y = 10d_p$ in all cases. In addition, simulations were carried out for systems with varying wedge angle θ_w, but the orifice width d_0 was correspondingly varied to keep r_1 constant, using the relation $d_0 = 2r_1 \sin(\theta_w/2)$ and for different r_2 (9, 12, 15, 18, 21 cm) to study the effect of height of filling in the hopper.

The two-dimensional spatial variation in the hopper of the volume fraction (ϕ), mean velocity ($\mathbf{v}$), and stress ($\boldsymbol{\sigma}$) are computed by using bins with a square cross-section of side d_p and depth L_y. The solid volume fraction is obtained from

$$\phi = \frac{1}{N}\sum_{i=1}^{N}\frac{V_{pi}}{V}, \tag{21}$$

where N is the number of particles in the bin, and V_{pi} and $V = d_p \times d_d \times L_y$ are the volume of particle i and bin volume, respectively. The mean velocity is given by

$$\mathbf{v} = \frac{1}{N}\sum_{i=1}^{N}\mathbf{v}_i, \tag{22}$$

where $\mathbf{v}_i$ is the instantaneous velocity of a particle i. The total stress tensor, composed of streaming and collisional components, is given by $\boldsymbol{\sigma} = \boldsymbol{\sigma}_s + \boldsymbol{\sigma}_c$ [29]. The streaming stress is given by [29]

$$\boldsymbol{\sigma}_s = \frac{1}{V}\sum_{i=1}^{N}(m_i \mathbf{C}_i \mathbf{C}_i), \tag{23}$$

where $\mathbf{C}_i = \mathbf{v}_i - \mathbf{v}_a$ is the fluctuation velocity of particle i, and $\mathbf{v}_a = \mathbf{v}(\mathbf{r}_i)$ is the mean velocity interpolated to the position of particle i ($\mathbf{r}_i$) [30]. The contact stress is given by

$$\boldsymbol{\sigma}_c = \frac{1}{V}\sum_{c=1}^{N_c}\mathbf{F}_{ij}\otimes\mathbf{r}_{ij}, \tag{24}$$

where $\mathbf{F}_{ij}$ is the interparticle force, $\mathbf{r}_{ij}$ is the vector joining the particle centres, $\otimes$ is the dyadic product, and the summation is over all particle-particle contacts (N_c) in the sampling volume V. Radial profiles of volume fraction [$\phi(r)$], velocity [$\mathbf{v}(r)$], and stress [$\boldsymbol{\sigma}(r)$] are computed similarly using Eqs. (21)–(24) for annular bins of height d_p, as shown in Fig. 1(a), and a bin volume $V = d_p \times (r\theta_w) \times L_y$.

A few simulations are also carried out for gravity-driven flow down a rough inclined plane to make rheological comparisons. The simulation volume dimensions are $L_x = 2\,\text{cm}$, $L_y = 1\,\text{cm}$, and $L_z = 6\,\text{cm}$, and periodic boundary conditions are applied in the x and y directions. The gravitational vector relative to the simulation volume is $\mathbf{g} = g\sin\nu\hat{\mathbf{e}}_x - g\cos\nu\hat{\mathbf{e}}_z$, where ν is the angle of inclination of the plane, and $\hat{\mathbf{e}}_x$ and $\hat{\mathbf{e}}_z$ are unit vectors in the x and z directions, respectively. Here, 6000 particles with properties corresponding to the base case are used in the simulations, and the inclined plane is made up of the same particles arranged on a square grid with particle separation equal to d_p. To create a rough base, the particles are displaced by a random distance in the range (0,d_p) in the z direction. More details of the system are given in Ref. [28]. The velocity profile [$v_x(z)$] and stress profiles [$\sigma_{xz}(z)$, $\sigma_{zz}(z)$] are obtained at steady state from which μ and I are computed. The simulations are carried out for different angles in the range $\nu \in (19.5^\circ, 24^\circ)$ at an interval of 0.5°. The simulations are repeated for $d_p = 2\,\text{mm}$ using a simulation box of dimensions $L_x = 4\,\text{cm}$, $L_y = 2\,\text{cm}$, and $L_z = 12\,\text{cm}$.

IV. RESULTS AND DISCUSSION

A. Flow characteristics

Figure 4 shows the spatial maps of the solid fraction (ϕ), radial velocity (v_r) with vectors, tangential velocity (v_θ), and stress components (σ_{rr}, $\sigma_{\theta\theta}$, $\sigma_{r\theta}$) for the base case (S_2, Table I). The shear rate ($\dot{\gamma}$), pressure (P), and the inertial number (I), computed from the data, are also shown in the figure. The radial velocity (v_r) increases in magnitude, and the velocity vectors converge toward the exit [Fig. 4(a)]. The solid fraction remains nearly constant and relatively high ($\phi > 0.57$) over the domain [Fig. 4(d)]. The spatial distribution of stress components (σ_{rr}, $\sigma_{\theta\theta}$) [Figs. 4(b) and 4(e)] indicate that both components are maximum at intermediate radial positions and are low at the free surface and exit. The tangential velocity and shear stress v_θ and $\sigma_{r\theta}$ [Figs. 4(c) and 4(f)] are negligibly small relative to v_r and σ_{rr} [Figs. 4(a) and 4(b)]. The shear rate [$\dot{\gamma}$, Fig. 4(g)] varies as the radial velocity (v_r), while the pressure [P, Fig. 4(h)] variation is like the normal stresses (σ_{rr}, $\sigma_{\theta\theta}$). The inertial number [I, Fig. 4(i)] is nearly constant over much of the domain but increases sharply near the free surface where the pressure is low and the exit where the shear rate is high and the pressure is low. The spatial distributions of all the variables shown in Fig. 4 indicate that there is no significant dependence on θ, and all the variables depend on radial distance r alone, as assumed in the theory. The behavior for the other cases studied (Table I) is qualitatively similar.

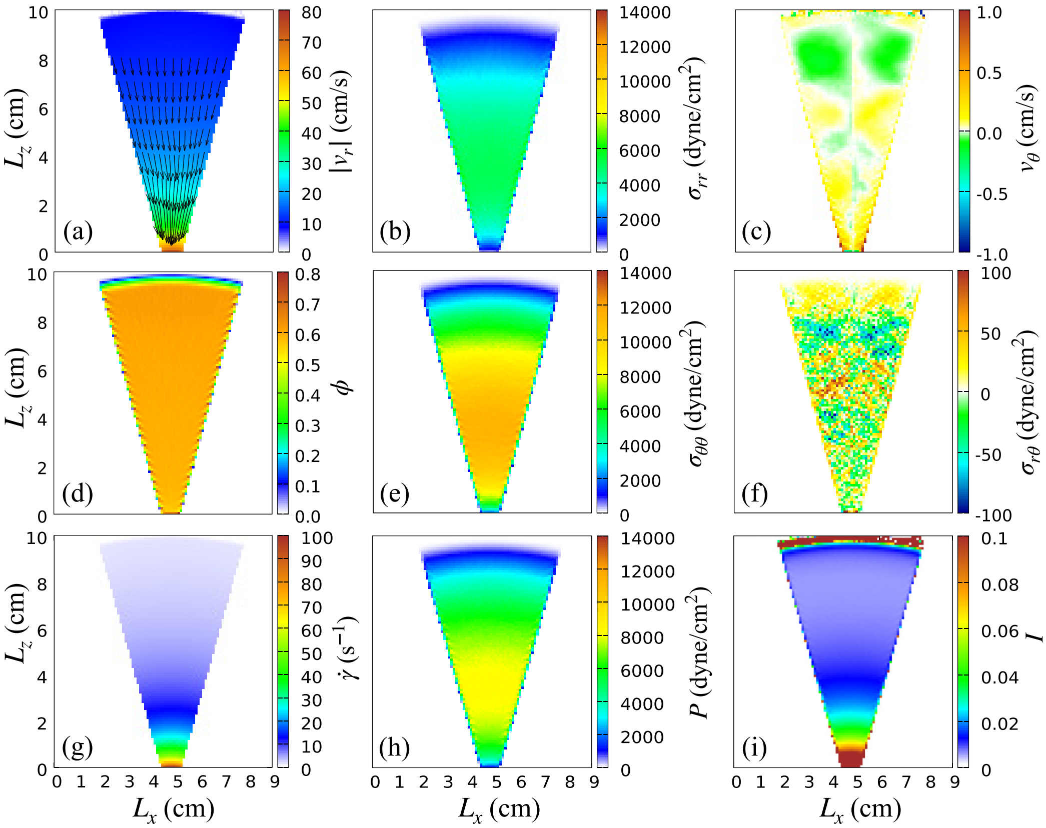

FIG. 4. Spatial distributions of flow variables. (a) Radial velocity (v_r), (b) radial stress (σ_{rr}), (c) tangential velocity (v_θ), (d) solid fraction (ϕ), (e) tangential stress ($\sigma_{\theta\theta}$), (f) shear stress ($\sigma_{r\theta}$), (g) shear rate ($\dot{\gamma}$), (h) pressure (P), and (i) inertial number (I). Parameter values used correspond to the base case (Table I).

B. Parametric study

Figure 5 shows the effect of the system geometrical parameters, orifice size (d_0), wedge angle (θ_w), and filling height (r_2), on the flow. Parameters, other than the ones varied, correspond to the base case (S_2, Table I). An increase in orifice size d_0 (Fig. 5, left column) results in higher particle velocities, lower solid fractions, and slightly lower stresses. This is consistent with the predictions of the Savage [16] model since an increase in d_0 keeping θ_w and r_2 fixed implies an increase in r_1/r_2. An increase in the wedge angle keeping the orifice width fixed (cases S_2, S_6–S_9) is equivalent to reducing r_1, and the trends are the same as reducing d_0 keeping θ_w fixed (data not shown). However, when the wedge angle is varied keeping r_1 and r_2 fixed, there is no significant change in any of the properties (Fig. 5, center column). Similar results are obtained for the pairs S_3, S_{22} and S_4, S_{23} for which the wedge angles are different but r_1 for each pair is the same (data not shown). The effect of filling height (r_2) on the maximum stress is significant [Fig. 5(k)], and the maximum stress increases more than twofold for a twofold increase in r_2. However, the velocity, solid fraction, and the stress are nearly unchanged. In all cases, the stress ratio k is nearly constant in the central region of the hopper and independent of the parameters varied, as required. In this region, $k \approx 2.28$, corresponding to an angle of internal friction of $\beta_s \approx 23^\circ$.

Figure 6 shows the effect of particle properties, coefficient of friction (μ_p), stiffness (k_n), and diameter (d_p), on the system behavior. Parameters, other than the one varied, correspond to the base case (S_2, Table I). Increase in the particle friction coefficient over a relatively wide range

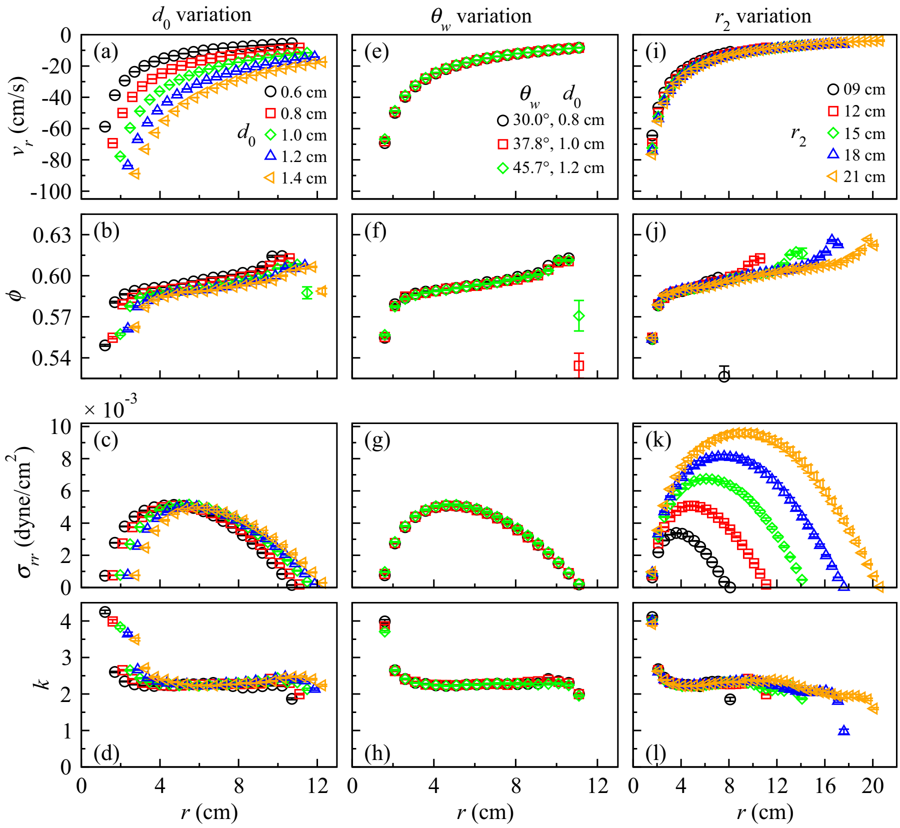

FIG. 5. Variation of the velocity (v_r), solid fraction (ϕ), stress (σ_{rr}), and stress ratio (k) with radial distance (r) for different hopper parameters. (a)–(d) Orifice width (d_0), (e)–(h) wedge angle (θ_w), and (i)–(l) height of material in the hopper (r_2). Parameters, other than the ones varied, correspond to the base case (Table I).

($\mu_p = 0$ to $\mu_p = 1$, Fig. 6, left column) results in a small decrease in the velocity, a significant decrease in the solid fraction and stress, and a significant increase in k. All the parameters (ϕ, v_r, σ_{rr}, and k) appear to saturate for particle friction values larger than about $\mu_p = 0.7$. The stress ratio ranges from $k = 1.44$ ($\beta_s = 10.4°$) for $\mu_p = 0$ to $k = 2.31$ ($\beta_s = 23.3°$) for $\mu_p = 1$. Thus, even frictionless particles have a significant internal friction angle. At the highest particle friction considered $\mu_p = 1$, the effective friction coefficient is $\tan \beta_s = 0.43$, which is much smaller than the interparticle friction. The variation in stiffness over three orders of magnitude has a negligible effect on the flow (Fig. 6, middle column). Increase in the particle diameter (Fig. 6, right column) results in a small decrease in the velocity but the other properties remain unchanged.

In all the cases shown in Figs. 5 and 6, there is a small increase in the volume fraction with increasing radial distance (r) of $\sim$ 3–5% over the entire range of r. Although the stress varies significantly with the radial distance, the stress ratio k is nearly constant over the domain except near the exit and the free surface. Therefore, the Savage [16] theory assumptions of constant density (ρ) and constant stress ratio (k) are reasonable for all these systems. However, the stress at the exit $\sigma_{rr}(r_1)$ is significant in magnitude in all cases [e.g., Fig. 6(c)], contrary to the assumption $\sigma_{rr}(r_1) = 0$ in the Savage [16] model.

Figure 7 shows the variation of the exit stress with hopper parameters (d_0, θ_w) and particle friction (μ_p) obtained from the computations. The exit stress reduces with increasing orifice size (d_0) and increasing friction coefficient (μ_p). The stress is nearly constant for increasing wedge angle (θ_w)

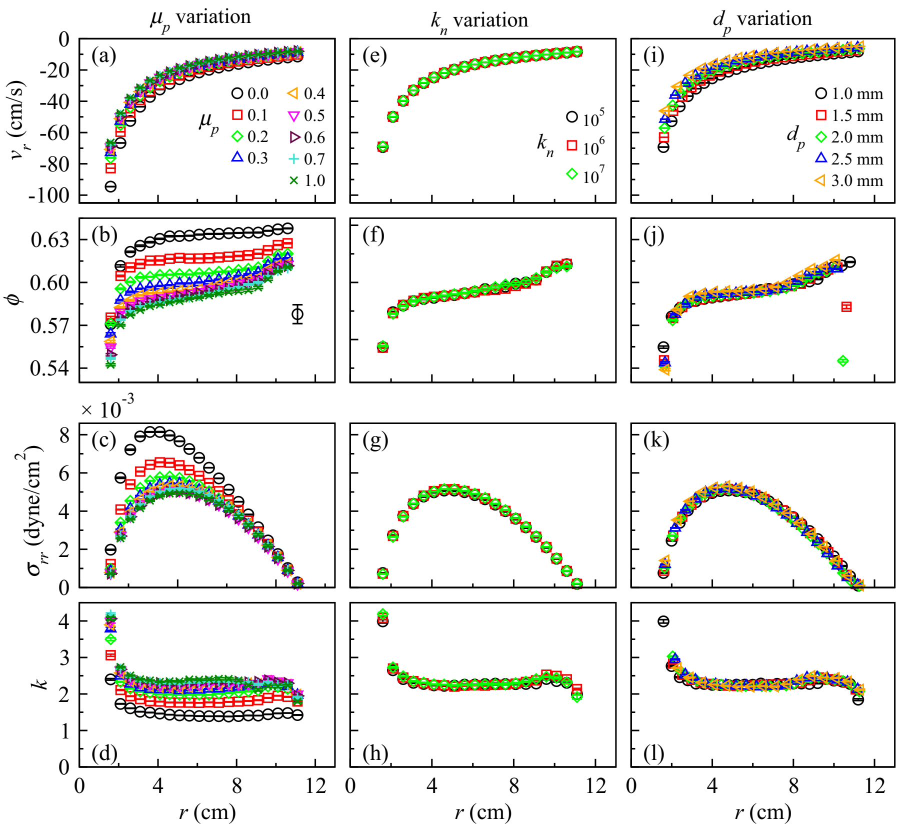

FIG. 6. Variation of the velocity (v_r), solid fraction (ϕ), stress (σ_{rr}), and stress ratio (k) with radial distance (r) for different particle parameters. (a)–(d) friction coefficient (μ_p), (e)–(h) stiffness (k_n), and (i)–(l) diameter (d_p). Parameters, other than the ones varied, correspond to the base case (Table I).

keeping orifice width fixed. The magnitude of the exit stress varies between 10 and 15% of the maximum stress in all the cases, and this has a significant impact on the flow rate, as shown below. Calculation of the stress at the exit is complex and needs a fully two-dimensional model.

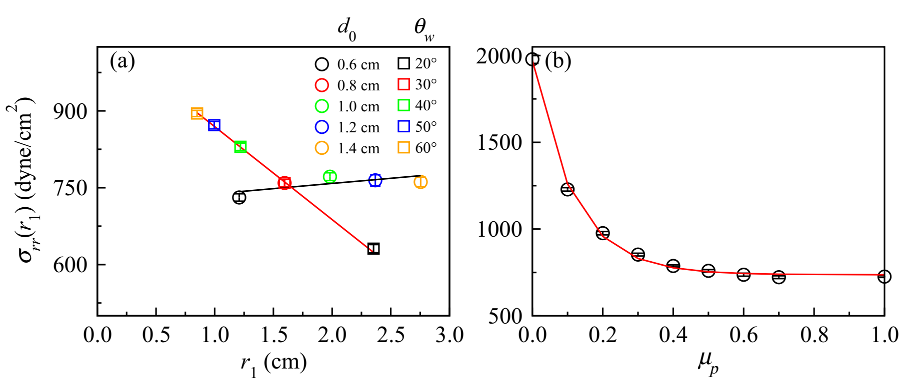

FIG. 7. Variation of the stress at the exit [$\sigma_{rr}(r_1)$] with system parameters. (a) Orifice width (d_0) and wedge angle (θ_w). The solid lines are straight line fits to the data. (b) Friction coefficient (μ_p). The solid line is an exponential fit to the data.

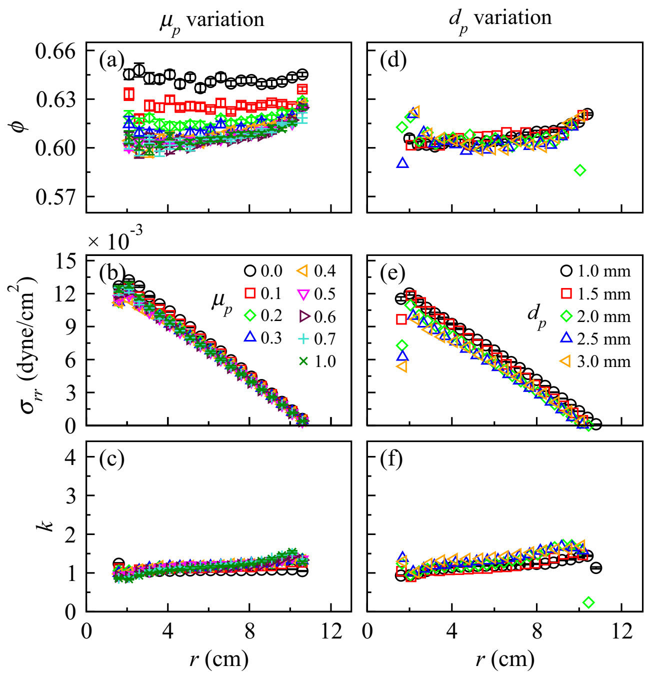

FIG. 8. Variation of the solid fraction (ϕ), stress (σ_{rr}), and stress ratio (k) with radial distance (r) under static conditions for different particle parameters. (a)–(c) friction coefficient (μ_p) and (d)–(f) diameter (d_p).

We finally present results for the static case. Figure 8 shows the solid fraction (ϕ), radial stress (σ_{rr}), and stress ratio (k) for the static bed with different particle friction coefficients (μ_p, left column) and particle diameters (d_p, right column). The solid fractions [Figs. 8(a) and 8(d)] decrease significantly with increasing particle friction coefficient (μ_p) are nearly independent of particle size (d_p). The magnitudes are close to those for the corresponding cases with flow [Figs. 6(b) and 6(j)]. However, the stress increases monotonically with depth [decreasing r, Figs. 8(b) and 8(e)] since the exit is closed, in contrast with a maximum in the profile obtained in the cases with flow [Figs. 6(c) and 6(k)]. The stress ratio (k) is nearly independent of particle friction coefficient [Fig. 8(c)], in contrast with the flow case where k increases significantly with particle friction (μ_p). The magnitude of the stress ratio is ~ 1 ($k = 1.21$) implying that the mobilization of interparticle friction is low, and the stress ratio corresponds to an angle of internal friction of $\beta_s = 5.5^\circ$, much smaller than that for the case for flow ($\beta_s = 23^\circ$).

C. Rheology

We obtain the parameters of the μ-I model from the computational results. From Eq. (17), the friction coefficient (μ) is obtained in terms of the stresses as

$$\mu = \frac{(\sigma_{\theta\theta} - \sigma_{rr})}{(\sigma_{\theta\theta} + \sigma_{rr})}. \tag{25}$$

Figure 9 shows the variation of μ and ϕ with the inertial number I for different d_0, θ_w, r_2, and k_n. The data collapse to a single curve for $I > 0.02$ for both μ and ϕ and are well described by the linear relations

$$\mu = \mu_s + aI, \tag{26}$$

$$\phi = \phi_0 - cI. \tag{27}$$

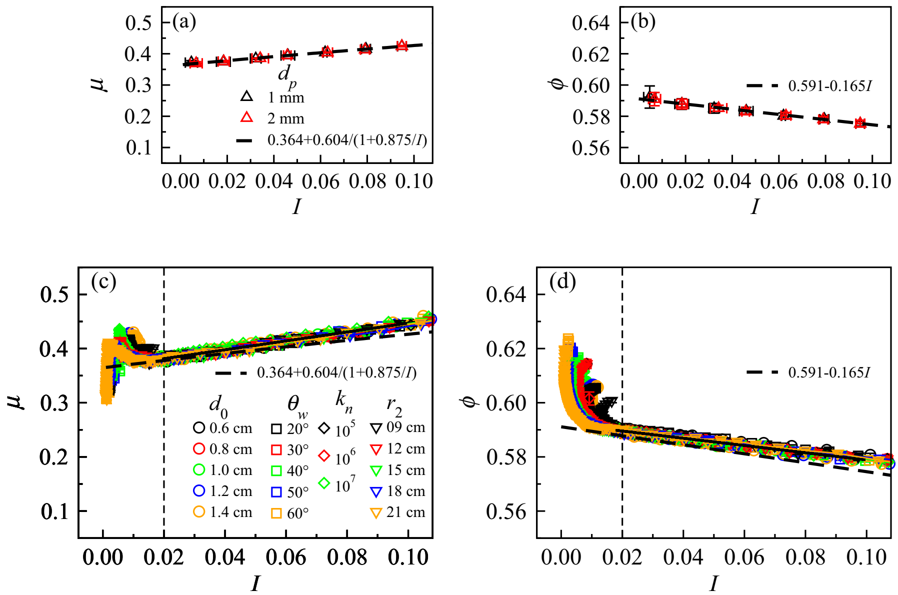

FIG. 9. Variation of (a) the friction coefficient (μ) and (b) the solid fraction (ϕ) with the inertial number (I) for flow down an inclined plane for two different particle diameters. The dashed lines are fits of Eqs. (27) and (28). Variation of (c) the friction coefficient (μ) and (d) the solid fraction (ϕ) with the inertial number (I) for hopper flow for different orifice widths (d_0), wedge angles (θ_w), stiffness (k_n), and heights of material in the hopper (r_2). Solid lines are fits of Eqs. (26) and (27). The fits for the inclined plane flow (dashed lines) are shown for comparison.

The fitted values of the coefficients (μ_s, a, ϕ_0, and c) are given in the Supplemental Material [31]. The deviation at low inertial numbers ($I < 0.02$) is a consequence of the very short time of flow, which may not be sufficient to achieve a steady state due to the low total strain [14]. The dashed line in Fig. 9(a) is the prediction of the Jop *et al.* [24] model

$$\mu = \mu_s + \frac{\mu_m - \mu_s}{1 + (I_0/I)}, \tag{28}$$

with the model parameters $\mu_s = 0.364$, $\mu_m = 0.968$, and $I_0 = 0.875$ obtained for the same particles for flow down a rough inclined plane for inertial numbers in the range $I \in (0.01, 0.13)$. Data for two different particle sizes ($d_p = 0.1, 0.2$ cm) and using the base case values of k_n, γ_n, and μ_p are shown in Figs. 9(a) and 9(b). The model predictions for shear flow are close to the data for the flow in the wedge but show a small but significant deviation at larger values of the inertial number (I). This indicates a weak dependence of the rheology on the flow type. Bhateja and Khakhar [15] found a similar deviation from the inclined plane flow rheology in a rectangular hopper flow.

Figure 10 shows the variation of the friction coefficient (μ) and the volume fraction (ϕ) with the inertial number (I) for different particle friction coefficients (μ_p) and particle diameters (d_p). Here, μ increases significantly and ϕ decreases significantly with increase in μ_p. The friction coefficient (μ) is nearly constant over the change in particle size [Fig. 10(c)], and the change in solid fraction is small [Fig. 10(d)]. The data show a linear variation for $I > 0.02$, and the lines are fits of Eqs. (26) and (27). The coefficients of the fitted equations (μ_s, a, ϕ_0, and c) are given in the Supplemental Material [31]. Here, R^2 values of ~0.99 are obtained in all the cases, indicating excellent fits. The fitted coefficients show a significant change only with the friction coeffcient μ_p, and this variation is shown in Fig. 11.

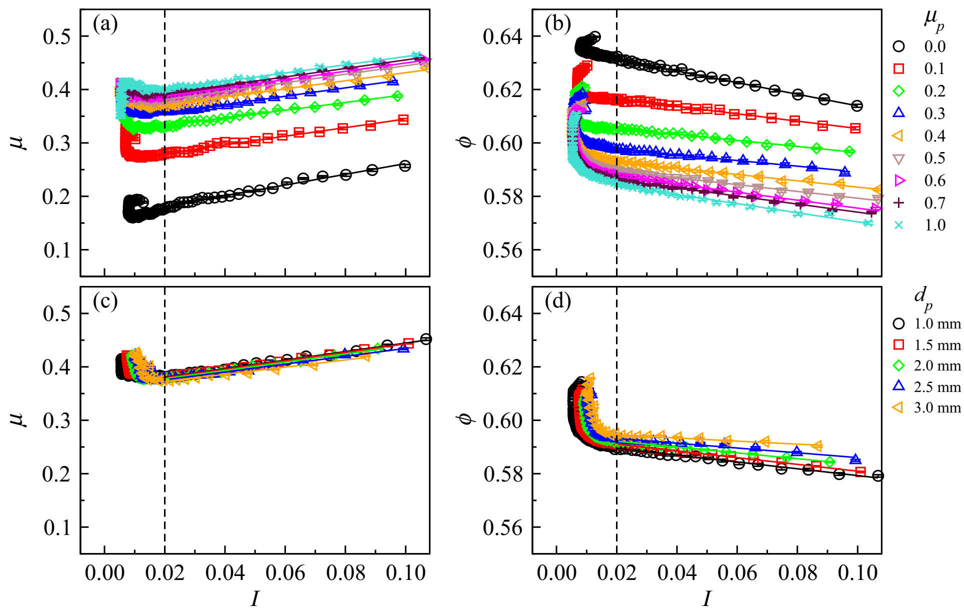

FIG. 10. Variation of (a) and (c) the friction coefficient (μ) and (b) and (d) the solid fraction (ϕ) with the inertial number (I) for different (a) and (b) particle friction coefficients (μ_p) and (c) and (d) particle diameters (d_p). Solid lines are fits of Eqs. (26) and (27).

D. Comparison with theoretical models

Consider first a comparison between the Savage [16] model and the μ-I model, for the computational results for the base case, shown in Fig. 12. For the Savage [16] model, the stress ratio k is obtained by fitting a horizontal line to the computed stress ratio data in the central region of the hopper [Fig. 12(d)], and the velocity and stress profiles are predicted using Eqs. (4), (8), and (11). In the case of the μ-I model, the constant A is obtained by fitting Eq. (4) to computational data for $v_r(r)$ [Fig. 12(a)], and the solid fraction, stress, and stress ratio profiles are predicted by numerical integration of Eq. (18) using the rheological parameters obtained in Sec. IV C and the boundary condition $\sigma_{rr}(r_2) = 0$. The fit of Eq. (4) to $v_r(r)$ data (R^2 of 0.99) and the match of the predictions of the μ-I model (solid lines) with data are excellent. The deviation of the theory from simulation data for the solid fraction [ϕ, Fig. 12(b)] in the region $r > 9$ cm is due to the low values of I in that region [$I < 0.02$, Fig. 9(d)], which prevents equilibration, as mentioned above. Since the hopper is filled by pouring from the top, the bed is slightly compressed. With flow, the bed expands to its equilibrium volume fraction given by the ϕ-I model. However, in the upper parts, where I is very low, the deformation is very small, and hence, the bed cannot achieve its equilibrium state.

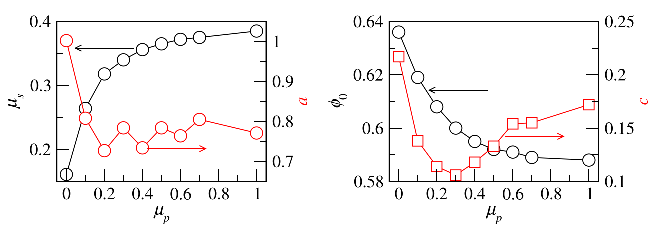

FIG. 11. (a) Variation of the fitted rheological parameters (μ_s, a) and (b) variation of the fitted solid fraction correlation parameters (ϕ_0, c) with the interparticle friction coefficient (μ_p).

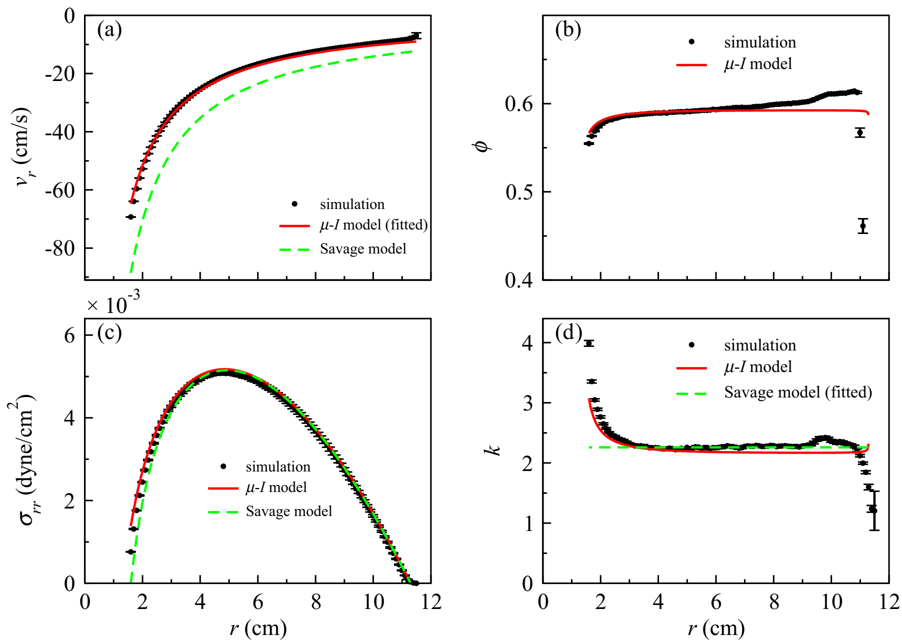

FIG. 12. Comparison of the profiles predicted by the Savage [16] model and the μ-I model to computational results for the base case. (a) Radial velocity (v_r), (b) solid fraction (ϕ), (c) radial stress (σ_{rr}), and (d) stress ratio (k).

In contrast with the μ-I model, the Savage [16] model (dashed lines) significantly overpredicts the velocity but predicts the stress profile very well, except for a significant deviation near the exit ($r = 1.6\,\mathrm{cm}$). The results indicate that the deviation of the velocity prediction of the Savage [16] model is not due to the wall friction, which is absent in the present case, but due to the boundary condition $\sigma_{rr}(r_1) = 0$. The finite stress at the exit results in a significant reduction in the velocity relative to the prediction from the Savage [16] model, in which the stress at the exit is assumed to be zero.

Figure 13 shows a comparison of the stress profile obtained by numerical integration of Eq. (18) to the approximate solution [Eq. (19)] and variants of the theory: the purely frictional case [$a = 0$ in Eq. (18)] and the case with inertia neglected [$\rho A^2/r^3$ terms omitted in Eq. (18)]. The approximate

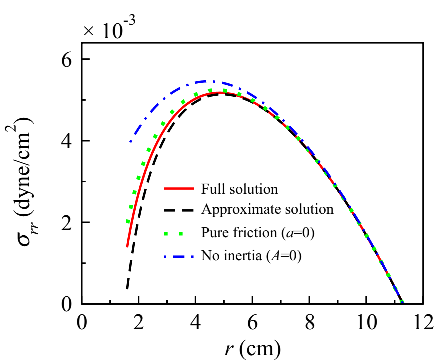

FIG. 13. Radial stress profiles predicted by the μ-I model for the base case for different approximations as indicated in the legend. Full solution: Eq. (18). Approximate solution: Eq. (19). Pure friction: Eq. (19) with $a = 0$. No inertia: Eq. (18) with $A = 0$.

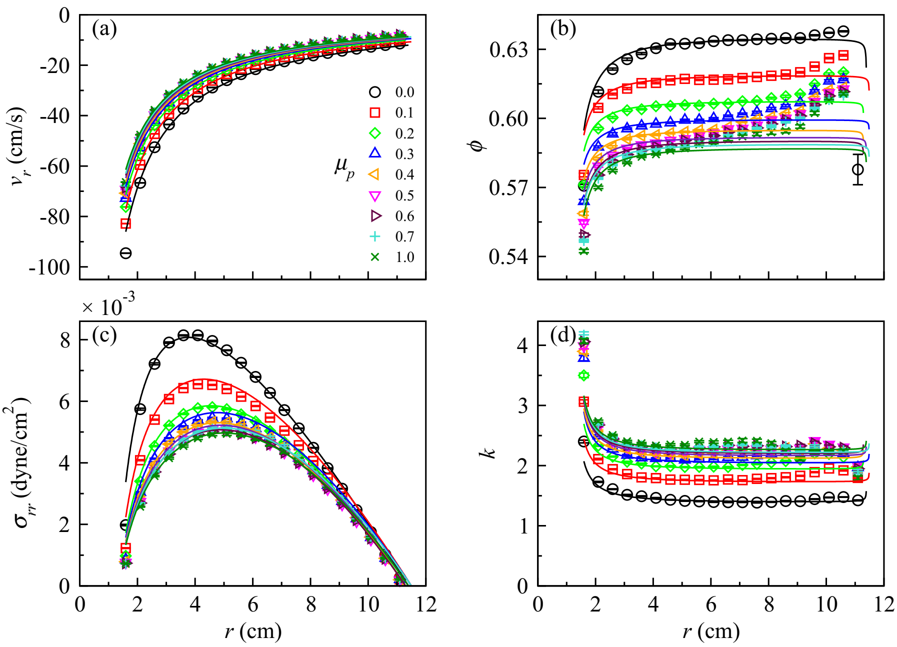

FIG. 14. Comparison of the profiles predicted by the μ-I model with computational results for the value of the particle friction coefficient (μ_p). (a) Radial velocity (v_r), (b) solid fraction (ϕ), (c) radial stress (σ_{rr}), and (d) stress ratio (k).

solution is close to the full solution. The purely frictional case, which corresponds to the Savage [16] model, but using a fitted value of A, gives good predictions of σ_{rr} except near the exit where collisional stresses become significant. Neglecting inertia results in a significant deviation, indicating that inertial stresses play an important role in the flow. However, a qualitatively similar profile with a maximum is obtained due to the viscous effects, in contrast with the Savage [16] model, which predicts monotonically increasing stress in the limit of negligible inertial stresses ($\rho A^2/r^3 = 0$).

Figure 14 shows the comparisons of the model predictions with computational results for different particle friction coefficients μ_p. The constant A was obtained by fitting Eq. (4) to the computational data for the radial velocity profile $v_r(r)$, and excellent fits are obtained in all cases [Fig. 14(a)], and fitted values for all cases are given in Table II. The predicted solid fraction (ϕ), radial stress (σ_{rr}), and stress ratio (k) profiles, using the fitted values of A and the μ-I model parameters obtained above, match very well with the computational results [Figs. 14(b)–14(d)]. The deviation of the solid fraction for $r > 9$ cm is for the same reason as discussed above for Fig. 12(b). Similar good agreement was obtained for all cases studied, and the fitted values of A [Eq. (4)] for each case are given in Table II. The fitted values k in the constant region along with values of A calculated from the Savage [16] model [Eq. (8)], using this fitted k value, for all cases are also given in Table II. The values predicted by the Savage [16] model for A are 36–100% higher than the fitted values (Table II).

Figure 15 shows the variation of the fitted values of the constant A with system parameters. The variation of A with r_1 and d_p is like that in the Beverloo correlation [3] and of the form $A \propto (r_1 - a_1 d_p)^{3/2}$ [fitted solid lines in Figs. 15(a) and 15(d)]. The constant decreases exponentially with increasing friction coefficient [fitted solid line in Fig. 15(b)] and varies with filling height (r_2) as $A \propto [1 - a_2(r_1/r_2)]$ [fitted solid line in Fig. 15(c)]. The correlation for A obtained from fitting is then

$$A = C_A g^{1/2}(r_1 - a_1 d_p)^{3/2}[1 - a_2(r_1/r_2)][1 + a_3 \exp(-\mu_p/\mu_{p0})], \tag{29}$$

TABLE II. Calculated values for constants A, k, and mass flow rates ($\dot{m}$) for sytems with varying orifice width (d_0), wedge angle (θ_w), friction coefficient (μ_p), stiffness values (k_n), damping coefficient (γ_n), radial distance (r_2), and particle diameter (d_p).

Systems	Parameters	k (fitted)	A (fitted)	A (Savage [16])	$\dot{m}$ in g/s (data)
Orifice width	d_0 in cm				
S_1	0.6	2.23	65.504	98.528	47.86
S_2	0.8	2.28	103.315	140.674	76.44
S_3	1.0	2.30	145.461	186.455	107.98
S_4	1.2	2.30	188.289	236.351	140.83
S_5	1.4	2.33	233.129	286.916	174.64
Wedge angle	θ_w				
S_6	20°	2.30	188.205	233.977	92.95
S_7	40°	2.25	65.713	99.280	64.47
S_8	50°	2.22	45.297	76.262	55.62
S_9	60°	2.18	33.396	62.657	49.03
Friction coefficient	μ_p				
S_{10}	0.0	1.44	137.296	188.776	106.50
S_{11}	0.1	1.82	123.019	163.539	94.47
S_{12}	0.2	2.05	114.030	150.716	86.29
S_{13}	0.3	2.18	108.780	145.245	81.51
S_{14}	0.4	2.25	105.717	141.692	78.42
S_{15}	0.6	2.31	101.678	139.215	74.82
S_{16}	0.7	2.31	100.459	139.661	73.78
S_{17}	1.0	2.31	98.065	139.439	71.63
Stiffness	k_n				
S_{18}	10^6	2.31	103.032	139.661	76.24
S_{19}	10^7	2.31	102.940	139.439	75.98
Wedge angle	θ_w, d_0 in cm				
S_{20}	37.8°, 1.0	2.29	102.194	140.029	95.45
S_{21}	45.7°, 1.2	2.27	100.711	140.855	114.15
S_{22}	23.9°, 0.8	2.30	145.761	185.436	85.98
S_{23}	19.9°, 0.8	2.29	190.197	233.109	93.35
Radial distance	r_2 in cm				
S_{24}	9	2.28	96.540	130.909	70.98
S_{25}	15	2.24	107.800	148.770	79.72
S_{26}	18	2.22	110.825	154.712	81.94
S_{27}	21	2.20	112.468	159.912	84.02
Paricle diameter	d_p in mm				
S_{28}	1.5	2.30	93.559	142.678	101.98
S_{29}	2.0	2.30	84.798	145.755	121.02
S_{30}	2.5	2.32	76.727	147.764	135.13
S_{31}	3.0	2.32	69.286	151.104	143.89

where the dimensionless fitted constants are $C_A = 2.29$, $a_1 = 1.63$, $a_2 = 1.31$, $a_3 = 0.38$, and $\mu_{p0} = 0.23$.

The parameter A is directly related to the mass flow rate by Eq. (10). Figure 16 shows the variation of the mass flow rate obtained from the simulations ($\dot{m}$, Table II) with $A\theta_w b$ using the fitted values

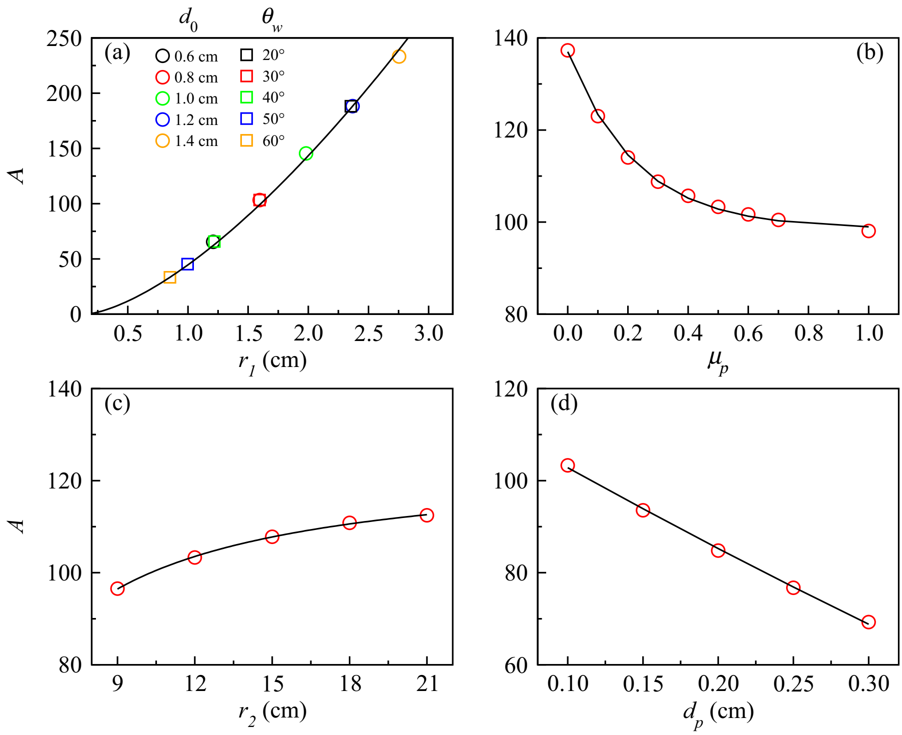

FIG. 15. Variation of the coefficient A with system parameters. (a) Exit radial distance (r_1) for varying orifice width (d_0) and wedge angle (θ_w), (b) particle friction coefficient (μ_p), (c) height of material in the hopper (r_2), and (d) particle diameter (d_p). Solid lines are fits of Eq. (29) to the data.

of A for all the data. A straight line with a slope $\rho = 1.43\,\text{g/cm}^3$ is obtained, giving an effective volume fraction at the exit of $\phi_1 = 0.57$, which is close to the values obtained from computations shown above.

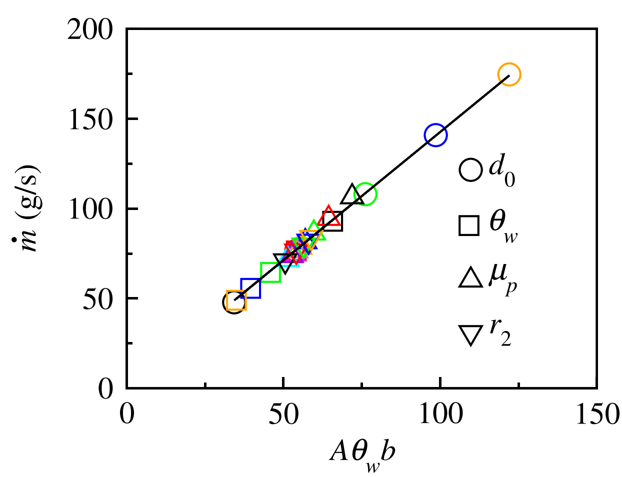

FIG. 16. Variation of the computed mass flow rate ($\dot{m}$) with $A\theta_w b$ for fitted values of A for different orifice width (d_0), wedge angle (θ_w), friction coefficient (μ_p), and heights of material in the hopper (r_2).

V. CONCLUSIONS

We presented results of DEM simulations in a wedge-shaped hopper with frictionless walls and radially directed gravity. The simulations show that the system closely conforms to the assumptions of the Savage [16] theory: The tangential velocity and shear stress are zero ($v_\theta \approx 0$, $\sigma_{r\theta} \approx 0$); all variables are independent of θ; and both bulk density ρ and stress ratio k are nearly constant.

A parametric study carried out on the system showed that the flow rate increases with orifice width (d_0), but the solid fraction (ϕ), stress (σ_{rr}), and stress ratio (k) are nearly unchanged. All variables are unchanged with change in the wedge angle when r_1 and r_2 are constant. Increase in the filling height (r_2) results in an increase in stress (σ_{rr}), but the velocity (v_r), solid fraction (ϕ), and stress ratio (k) are nearly unchanged. Increase in the particle friction coefficient results in a significant reduction in the solid fraction and stress, a relatively small reduction in the flow rate, and a significant increase in the stress ratio. All parameters saturate for $\mu_p > 0.7$. Increase in the particle stiffness has a negligible effect on the flow variables, and increase in the particle diameter results in a small reduction in the velocity, but the other parameters are nearly unchanged. The stress ratio ranges from $k = 1.44$ ($\tan \beta_s = 0.18$) for $\mu_p = 0$ to $k = 2.31$ ($\tan \beta_s = 0.43$) for $\mu_p = 1$. Thus, even frictionless particles have a significant internal friction, and at higher values of the particle friction, the internal friction is lower than the particle friction. Under static conditions, all flow variables are nearly independent of the system parameters except the solid fraction which reduces significantly with increase in the particle friction coefficient. The stress ratio is about $k = 1.21$ ($\beta_s = 5.5^\circ$) and independent of the particle friction coefficient, indicating that the mobilization of friction is low compared with the flowing particles.

The parametric study also shows a significant stress at the hopper exit [$\sigma_{rr}(r_1) \gg 0$] in all cases (~10–15% of the maximum stress), which is contrary to the assumption of zero stress at the exit [$\sigma_{rr}(r_1) = 0$] in the Savage [16] model. The finite stress at the exit for the base case results in a 36–100% lower flow rate compared with the Savage [16] model for the different parameters studied.

The velocity in the system is shown to be purely radial and corresponds to an extensional flow. The μ-I model is found to describe the rheology of the flow very well for inertial numbers $I > 0.02$ for all cases considered. The $\mu(I)$ function for the wedge flow shows a small but significant difference relative to the function for shear flow, indicating a small dependence of the rheology on the flow type. However, the deviation is small, implying that rheological data for shear flow may be used in a more complex flow, such as a hopper flow, with reasonable accuracy.

The μ-I model gives very good predictions of the solid fraction, stress, and stress ratio using a fitted value of the constant A. The model predicts a maximum in the stress profile, even in the absence of inertial stresses; however, the latter have a significant effect on the flow. The Savage [16] model gives good predictions of the stress, except at the exit, but significantly overpredicts the velocity using a fitted value of k. In addition to validating the μ-I rheology for hopper flow, we also show the applicability of the Shield-Jenike equation (Mohr-Coulomb condition) for predicting the stress profile in a hopper. A correlation for the velocity constant A is presented in terms of the system parameters, and the mass flow rate from the simulations is shown to agree well with that computed using the fitted values of A.

The results presented in this paper indicate that accurate prediction of the flow rate in the hopper requires an estimate of the stress at the exit for a hopper with frictionless walls. Nonzero exit stresses are also obtained for the more realistic case of a hopper with frictional walls, as shown for one case in Fig. 17. Estimating the exit stress requires an analysis of the two-dimensional flow in the region near the exit, which is complex. An alternate approach, used in this paper, is to estimate the flow rate independently, perhaps using a correlation, and use the flow rate to obtain the unknown constant of integration in the analysis instead of using the exit stress boundary condition. Frictional walls would reduce the flow rate, and hence, the correlation for the velocity constant A [Eq. (29)] would not be directly applicable to the case of a hopper with frictional walls, although a similar equation could be developed.

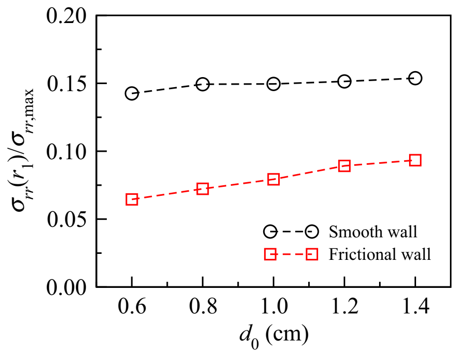

FIG. 17. Variation of the ratio of the exit stress to the maximum stress $[\sigma_{rr}(r_1)/\sigma_{rr,\max}]$ with orifice width (d_0) for frictionless walls and frictional walls with a wall friction coefficient $\mu_w = 0.5$. Parameters correspond to the base case (Table I).

In this paper, we also show the utility of the smooth-wall, radial-gravity, wedge-shaped hopper flow as a model extensional flow for computational evaluation of rheological models.

ACKNOWLEDGMENTS

Partial financial support was received from the Science and Engineering Research Board, India, Grant No. SPR/2020/000301. We dedicate this work to the memory of Professor Stuart L. Savage.

DATA AVAILABILITY

The data that support the findings of this article are openly available [32].

[1] D. Schulze, *Powders and Bulk Solids: Behavior, Characterization, Storage and Flow*, 2nd ed. (Springer Nature, Switzerland AG, 2021).

[2] R. Brown and J. Richards, Two-and three-dimensional flow of grains through apertures, Nature (London) **182**, 600 (1958).

[3] W. A. Beverloo, H. A. Leniger, and J. Van de Velde, The flow of granular solids through orifices, Chem. Eng. Sci. **15**, 260 (1961).

[4] A. W. Jenike, Steady gravity flow of frictional-cohesive solids in converging channels, J. Appl. Mech. Trans. ASME **31**, 5 (1964).

[5] R. M. Nedderman, U. Tüzün, S. B. Savage, and G. T. Houlsby, Flow of granular materials—I. Discharge rates from hoppers, Chem. Eng. Sci. **37**, 1597 (1982).

[6] S. M. Rubio-Largo, A. Janda, D. Maza, I. Zuriguel, and R. C. Hidalgo, Disentangling the free-fall arch paradox in silo discharge, Phys. Rev. Lett. **114**, 238002 (2015).

[7] F. Alonso-Marroquin and P. Mora, Beverloo law for hopper flow derived from self-similar profiles, Granular Matter **23**, 7 (2021).

[8] R. M. Nedderman, *Statics and Kinematics of Granular Materials* (Cambridge University Press, Cambridge, 1992).

[9] R. O. Uñac, A. M. Vidales, O. A. Benegas, and I. Ippolito, Experimental study of discharge rate fluctuations in a silo with different hopper geometries, Powder Technol. **225**, 214 (2012).

[10] S. Albaraki and S. J. Antony, How does internal angle of hoppers affect granular flow? Experimental studies using digital particle image velocimetry, Powder Technol. **268**, 253 (2014).

[11] D. Méndez, R. C. Hidalgo, and D. Maza, The role of the hopper angle in silos: Experimental and CFD analysis, Granular Matter **23**, 34 (2021).
[12] Z. Zou, P. Ruyer, P.-Y. Lagrée, and P. Aussillous, Nonsteady discharge of granular media from a silo driven by a pressurized gas, Phys. Rev. Fluids **7**, 064306 (2022).
[13] R. M. Gandia, F. C. Gomes, W. C. de Paula, and P. J. A. Rodriguez, The influence of flow pattern and hopper angle on static and dynamic pressures in slender silos, Powder Technol. **427**, 118756 (2023).
[14] C. H. Rycroft, K. Kamrin, and M. Z. Bazant, Assessing continuum postulates in simulations of granular flow, J. Mech. Phys. Solids **57**, 828 (2009).
[15] A. Bhateja and D. V. Khakhar, Analysis of granular rheology in a quasi-two-dimensional slow flow by means of discrete element method based simulations, Phys. Fluids **32**, 013301 (2020).
[16] S. B. Savage, The mass flow of granular materials derived from coupled velocity-stress fields, Br. J. Appl. Phys. **16**, 1885 (1965).
[17] S. B. Savage, Gravity flow of a cohesionless bulk solid in a converging conical channel, Int. J. Mech. Sci. **9**, 651 (1967).
[18] C. Brennen and J. C. Pearce, Granular materialflow in two-dimensional hoppers, J. Appl. Mech. **45**, 43 (1978).
[19] K. R. Kaza and R. Jackson, The rate of discharge of coarse granular material from a wedge-shaped mass flow hopper, Powder Technol. **33**, 223 (1982).
[20] S. B. Savage and M. Sayed, Gravity flow of coarse cohesionless granular materials in conical hoppers, J. Appl. Math. Phys. **32**, 125 (1981).
[21] J. R. Prakash and K. K. Rao, Steady compressible flow of granular materials through a wedge-shaped hopper; the smooth wall, radial gravity problem, Chem. Eng. Sci. **43**, 479 (1988).
[22] A. N. Schofield and P. Wroth, *Critical State Soil Mechanics* (McGraw-Hill, London, 1968), Vol. 310.
[23] R. Jyotsna and K. K. Rao, A frictional-kinetic model for the flow of granular materials through a wedge-shaped hopper, J. Fluid Mech. **346**, 239 (1997).
[24] P. Jop, Y. Forterre, and O. Pouliquen, A constitutive law for dense granular flows, Nature (London) **441**, 727 (2006).
[25] A. W. Jenike and R. Shield, On the plastic flow of Coulomb solids beyond original failure, J. Appl. Mech. **26**, 599 (1959).
[26] R. Jyotsna and K. K. Rao, Steady incompressible flow of cohesionless granular materials through a wedge-shaped hopper: Frictional-kinetic solution to the smooth wall, radial gravity problem, Chem. Eng. Sci. **46**, 1951 (1991).
[27] A. P. Thompson, H. M. Aktulga, R. Berger, D. S. Bolintineanu, W. M. Brown, P. S. Crozier, P. J. in 't Veld, A. Kohlmeyer, S. G. Moore, T. D. Nguyen *et al.*, LAMMPS—A flexible simulation tool for particle-based materials modeling at the atomic, meso, and continuum scales, Comput. Phys. Commun. **271**, 108171 (2022).
[28] L. E. Silbert, D. Ertaş, G. S. Grest, T. C. Halsey, D. Levine, and S. J. Plimpton, Granular flow down an inclined plane: Bagnold scaling and rheology, Phys. Rev. E **64**, 051302 (2001).
[29] J. T. Jenkins and S. B. Savage, A theory for the rapid flow of identical, smooth, nearly elastic, spherical particles, J. Fluid Mech. **130**, 187 (1983).
[30] R. Artoni and P. Richard, Average balance equations, scale dependence, and energy cascade for granular materials, Phys. Rev. E **91**, 032202 (2015).
[31] See Supplemental Material at http://link.aps.org/supplemental/10.1103/PhysRevFluids.10.034303 for LAMMPS scripts used for the simulations, data generated from the simulation, and value of the fitted rheological parameters.
[32] A. Momin, Discrete element method simulation data for granular flow in a wedge-shaped hopper [data set], Zenodo (2025),10.5281/zenodo.15009571.